CHAPTER 3

METHODS

3.1 Workflow

The workflow (**Figure 3.1**) used in this study is divided into 6 main phases as follows:

1. Conditioning input data and estimating S-wave velocity (Chapter 1)
2. Performing well-to-seismic tie and new elastic log generation
3. Performing AVO gradient analysis to create the intercept (A) and gradient (B) volumes
4. Determining the optimum chi angle for different rock elastic parameters
5. Building EEI model, extracting wavelets, and subsequently performing EEI inversion
6. Inverting EEI reflectivity volumes to impedance (EEI) volumes

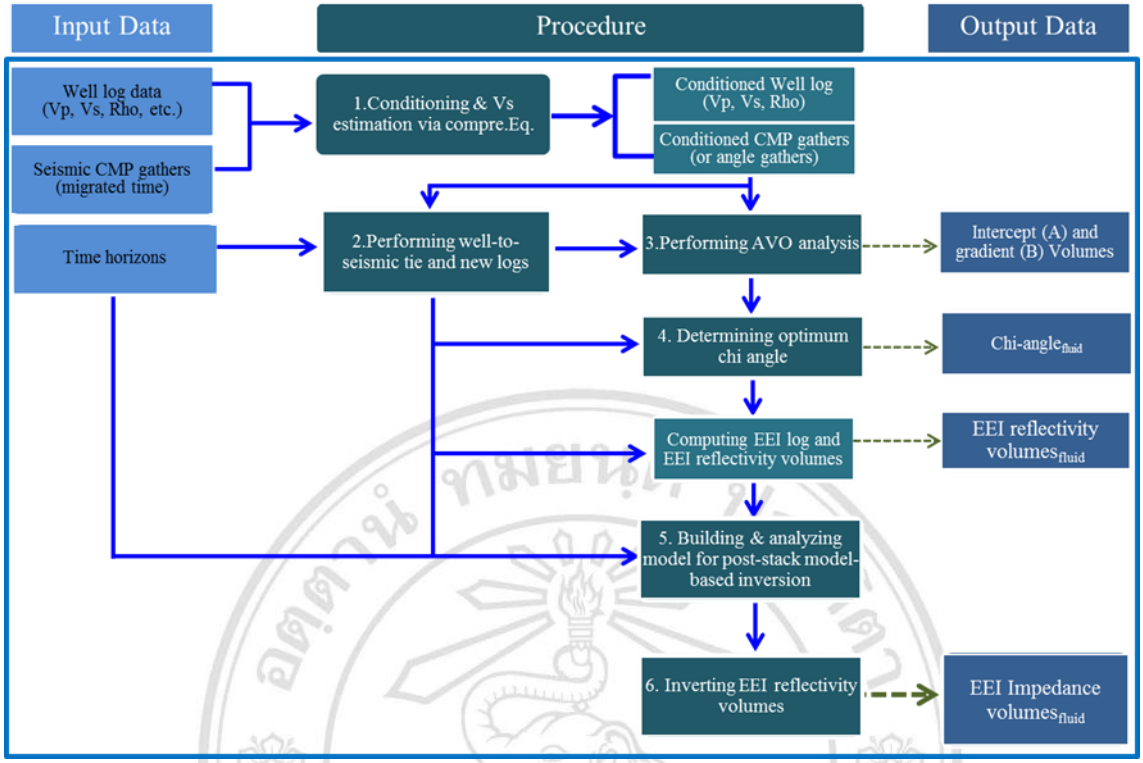

Figure 3.1. Simplified workflow describing briefly procedures used in this study.

3.1.1 Petrophysical reviews

Based on the comprehensive petrophysical evaluations from final well reports, the lithology, reservoir and net pay (i.e. the net thickness of economical hydrocarbon-filled reservoirs) determinations were done by using cut-off parameters as follows:

Lithology:	Limestone	VCL ≤ 30 %
	Thickness	≥ 0.5 m
	Shale	VCL > 30%
Reservoir:	Porosity	≥ 3%

The petrophysicist or others who determined the net pay also took gas show, water saturation and pressure gradient (if available) into account. In this study, there are 3 wells of hydrocarbon proven reservoirs which are well A1, well A2, and well A4. It is water bearing at well A8 (**Figure 3.2-Figure 3.5**). From **Figure 3.2** to **Figure 3.4**, the hydrocarbon zones were indicated by green box, which represent oil zones. Although the gas-bearing reservoirs were proven in the Shuaiba formation, but they had not been focused in this study.

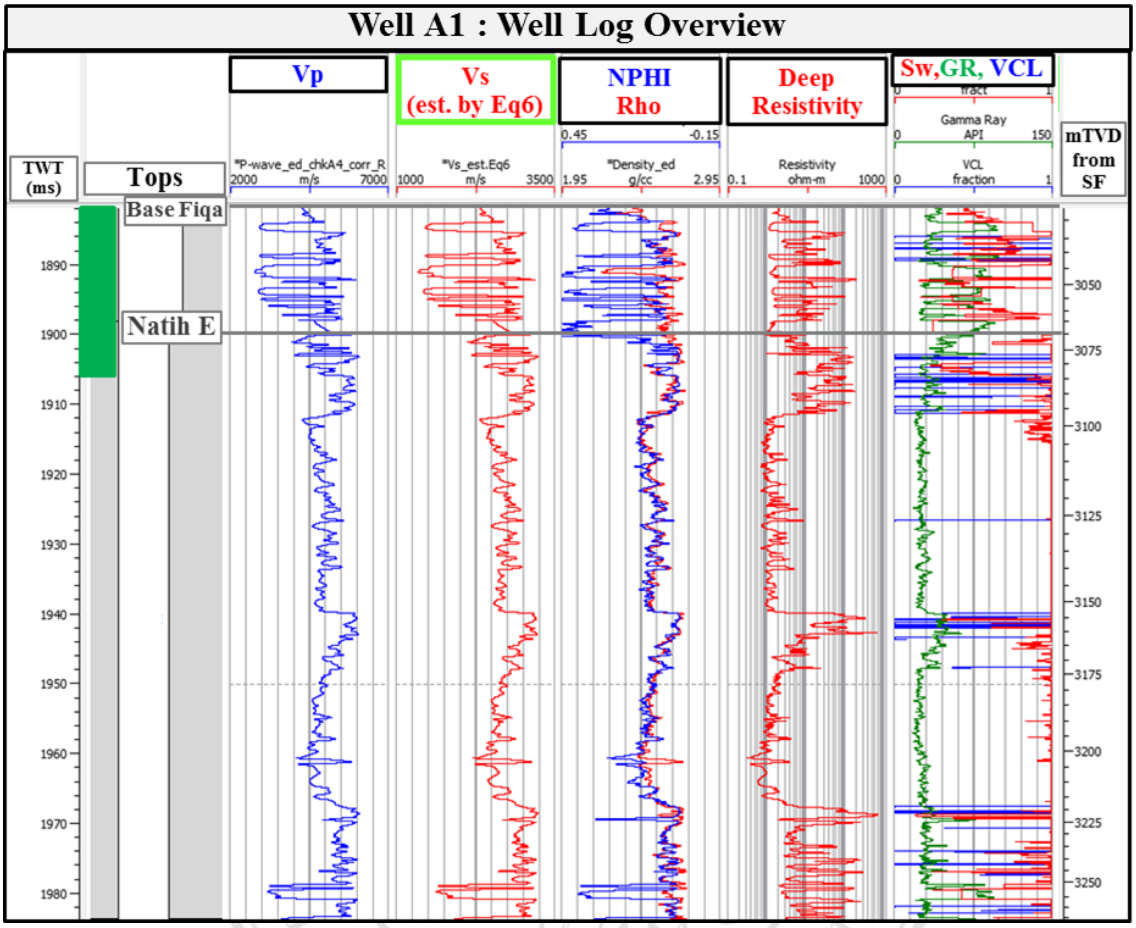

Figure 3.2. The log display for well A1 showing (from left to right) P-wave and S-wave velocities (Vp & Vs), Neutron porosity and density (NPHI & Rho), deep resistivity, and water saturation, GR, and volume of clay (Sw, GR, & VCL) respectively. The green box represents the oil zones.

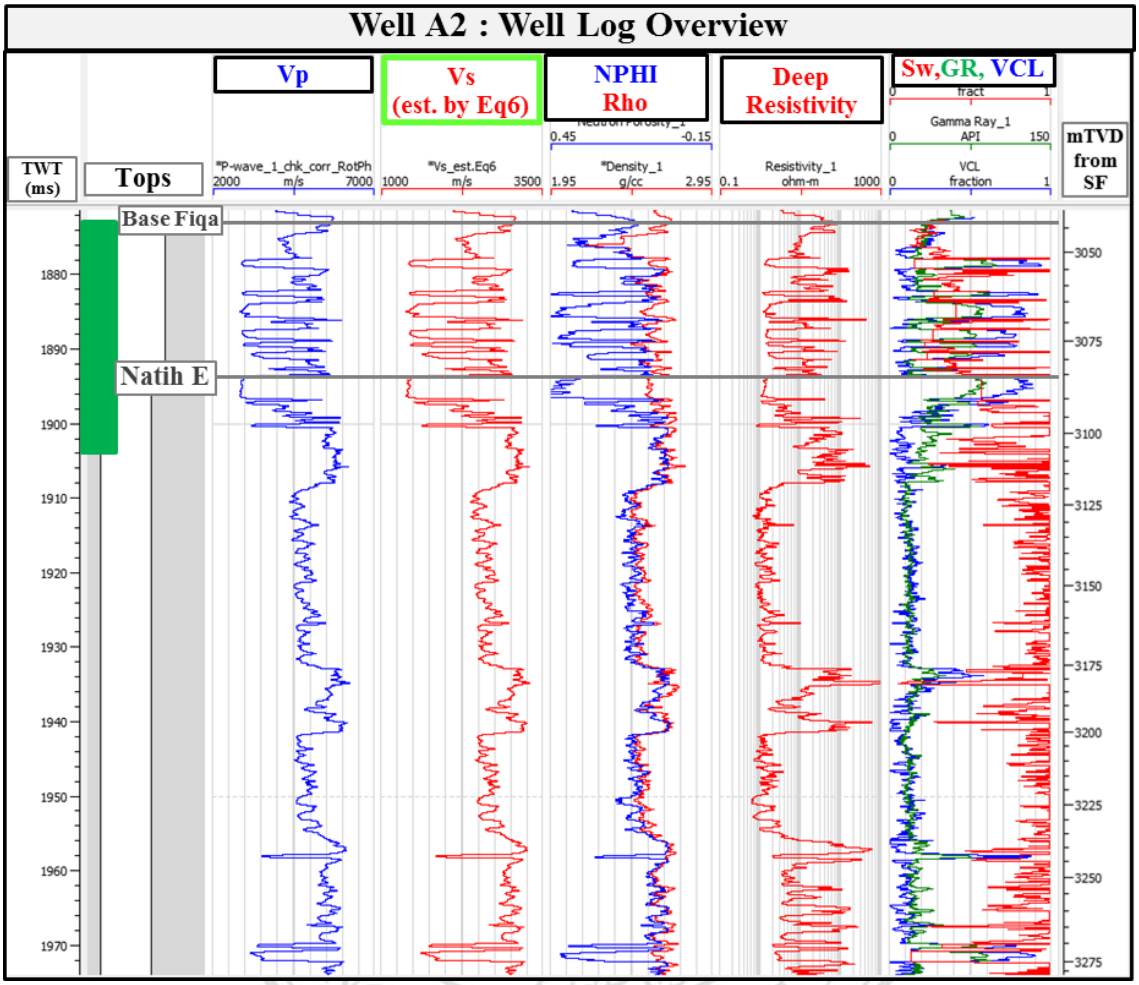

Figure 3.3. The log display for well A2 showing (from left to right) P-wave and S-wave velocities (Vp & Vs), Neutron porosity and density (NPHI & Rho), deep resistivity, and water saturation, GR, and volume of clay (Sw, GR, & VCL) respectively. The green box represents the oil zones.

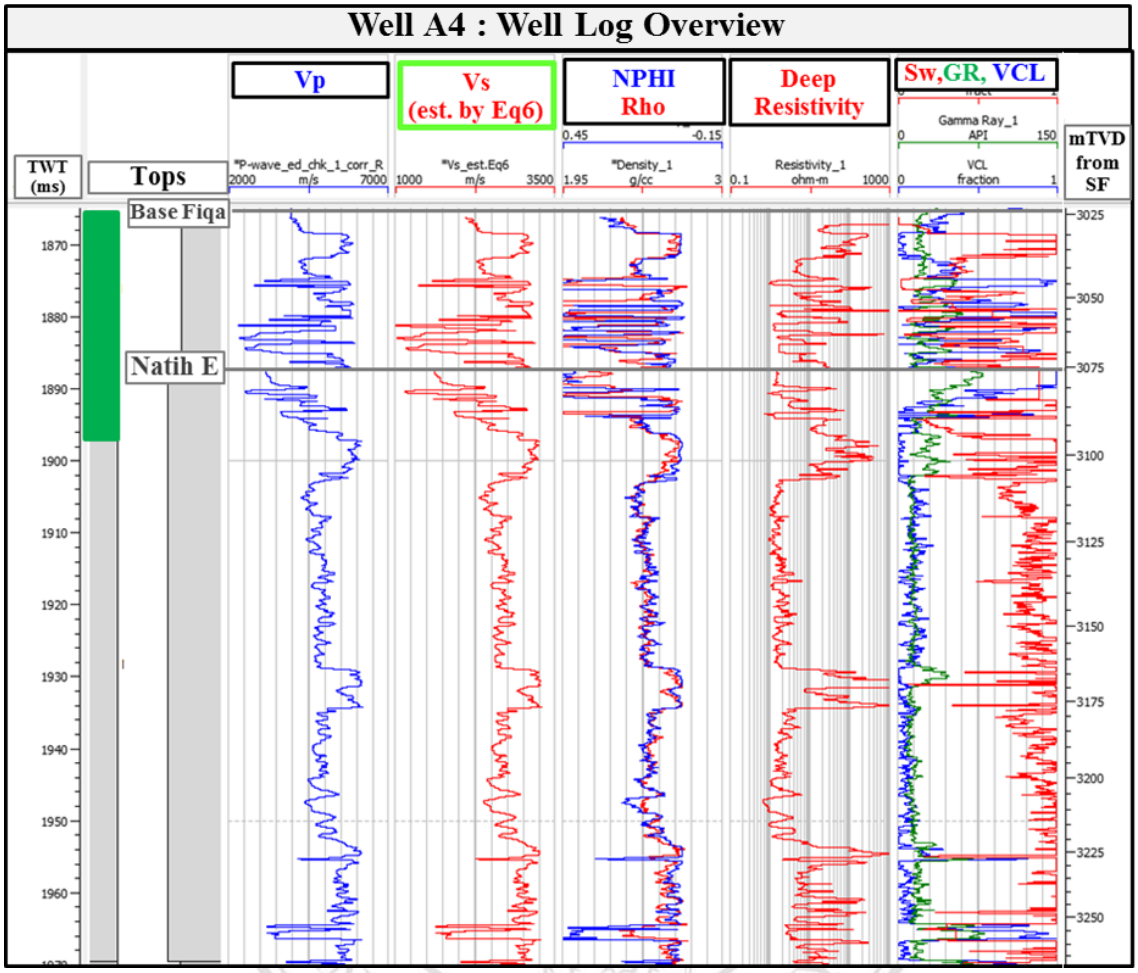

Figure 3.4. The log display for well A4 showing (from left to right) P-wave and S-wave velocities (Vp & Vs), Neutron porosity and density (NPHI & Rho), deep resistivity, and water saturation, GR, and volume of clay (Sw, GR, & VCL) respectively. The green box represents the oil zones.

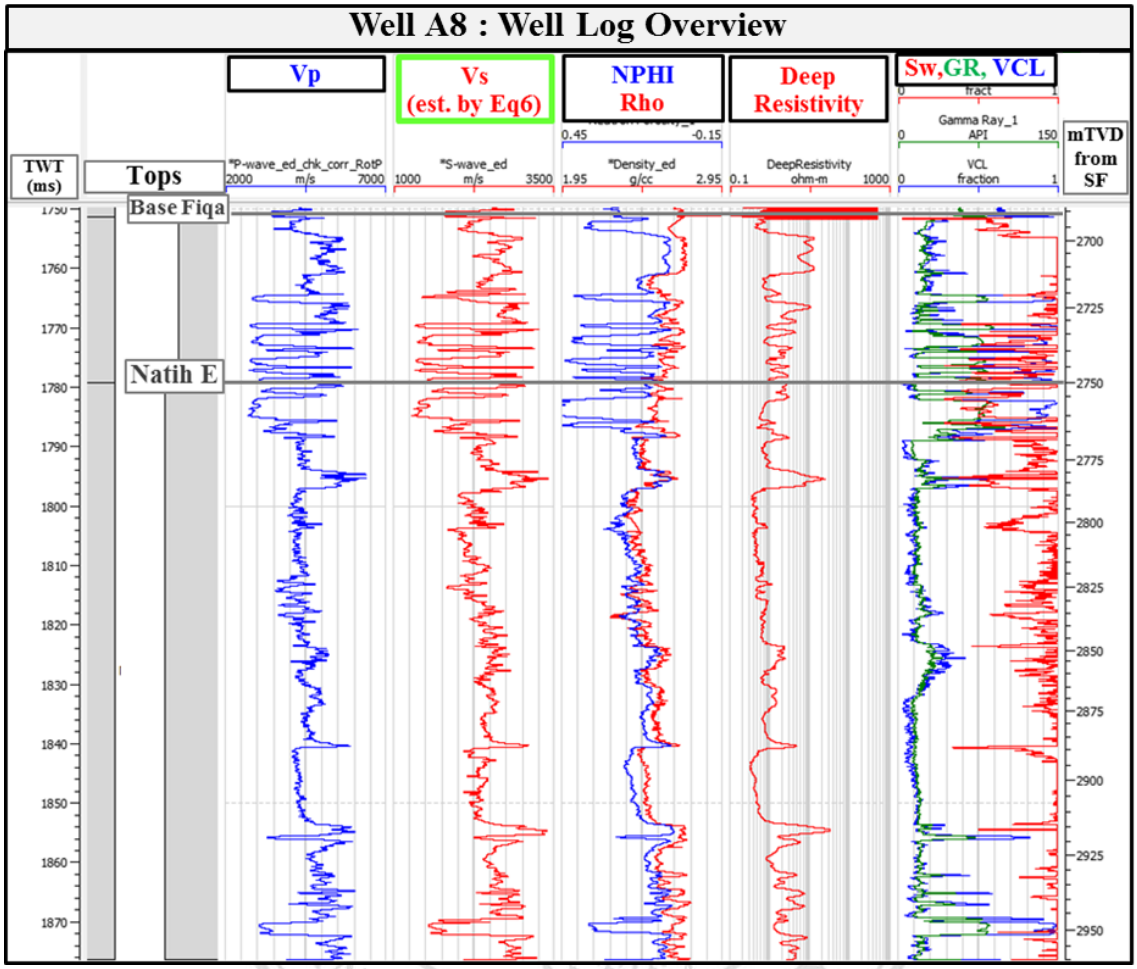

Figure 3.5. The log display for well A8 showing (from left to right) P-wave and S-wave velocities (Vp & Vs), Neutron porosity and density (NPHI & Rho), deep resistivity, and water saturation, GR, and volume of clay (Sw, GR, & VCL) respectively. This well is water bearing reservoirs.

3.2 Well-to-seismic ties and new elastic log generation

After data checking had been performed as presented in section 1.5 of Chapter 1, the well-to-seismic ties of 4 wells are performed. Well A8 is the main important which it is selected to do firstly and then well A1, A2, and A4 accordingly. All the depths in this study are in meters true vertical depth below surface (m TVDSF), unless if specified (**Figure 3.6**). The kelly bushing (KB) elevation is 10 m above surface and the elevations of KB at well A1, A2, A4, and A8 are 212.20, 213.30, 212.40, and 202.90 m respectively.

The check shot surveys were acquired and recorded by using seismic reference datum (SRD) at 122 m above mean sea level (MSL) at which the replacement velocity is approximately 2133 m/s.

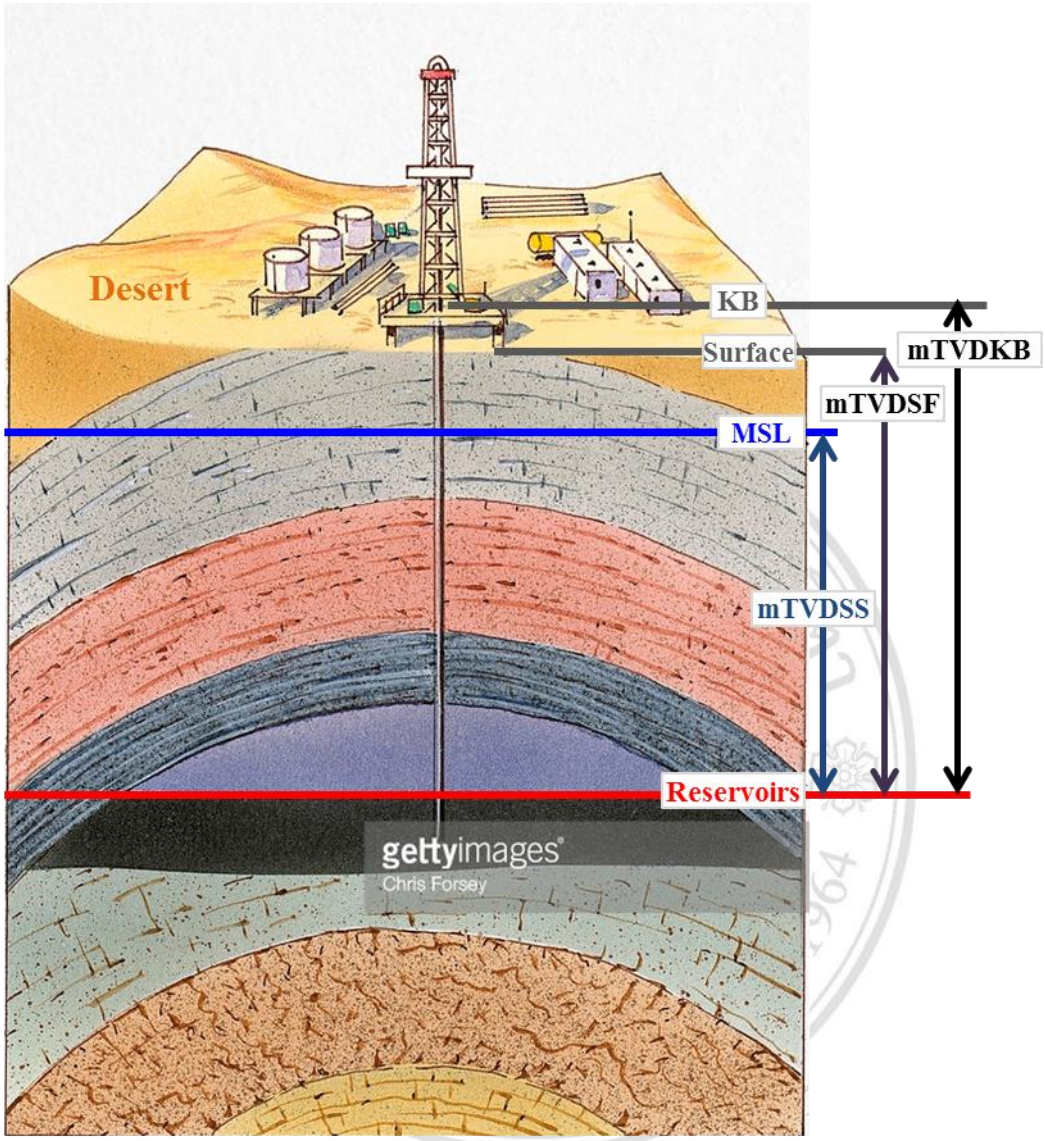

From http://www.gettyimages.co.uk

Figure 3.6. Schematic showing the meters true vertical depth (mTVD) measurements in general at which the mTVDSF (meters true vertical depth below surface) would be used in this study (modified from Forsey, C., 2016)

3.2.1 Well-to-seismic ties

To compare the well logs to the seismic data, check shot calibration was performed at all four wells (**Figure 3.7**), that the sonic log was calibrated based on check shot data. From **Figure 3.7**, the zone of interest at each well is highlighted by pink arrows and the large amount of drift curve is indicated by red ovals that might cause by these possibilities such as the use of pseudo-check shot from other well location and the velocity variations across the area.

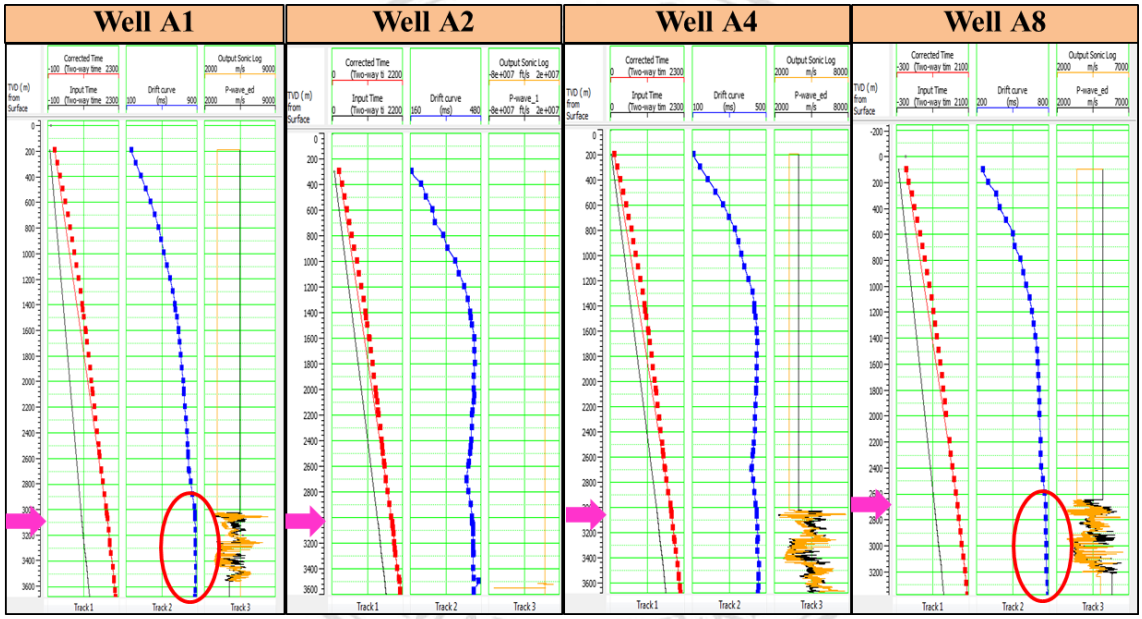

Figure 3.7. The schematic showing check shot calibration at well A1, A2, A4 and A8 (from left to right).

To accomplish the well-to-seismic tie, the conditioned P-wave velocity and density logs were computed to obtain the acoustic impedance and reflectivity accordingly, and then the reflectivity convolves with selected wavelet to generate the synthetic seismogram having the reversed polarity which was illustrated in **Figure 3.8**. The data shows the European polarity which the increase in impedance (+ve reflectivity) corresponding to the trough.

There are 2 basic methods of wavelet extraction in the Hampson-Russell software including first method integrates the wells to extract from desired seismic volume, and second method extracts from seismic volume alone, that is called statistical wavelet. The wavelet uses the wells, former method, can provide a good estimate of both amplitude and phase spectra (Hampson and Russell, 2015). However, that former method can be used after the well was already correlated or tied to seismic data. In the latter method, one must make an assumption about the phase of wavelet, which is typically zero-phase. The other ways of wavelet generation is to create the analytical wavelet such as Ricker wavelet and Bandpass wavelet in which the frequency, phase and length of wavelet will be set manually.

In **Figure 3.8**, there are the panels of well logs, computed acoustic impedance (AI) and reflectivity (R), and comparisons among three seismic correlation panels (synthetic seismograms in blue: Syn. and composite seismic traces in red: Comp.) derived by different wavelets, which are statistical CMP wavelet extracted from pre-stack CMP gathers (pink box), statistical PSTM extracted from 2013 post-stack time migration (light green box), and analytical Ricker created at 40 Hz (Blue box) wavelets. All synthetics were set as the reversed polarity. It is significantly depicted that the maximum correlation coefficient (0.56 at time shift -10 ms) can obtain by using statistical CMP wavelet extracted from pre-stack CMP gathers (pink box). Therefore, the statistical wavelet from CMP gathers was selected to be used as starting point for synthetic seismogram generation.

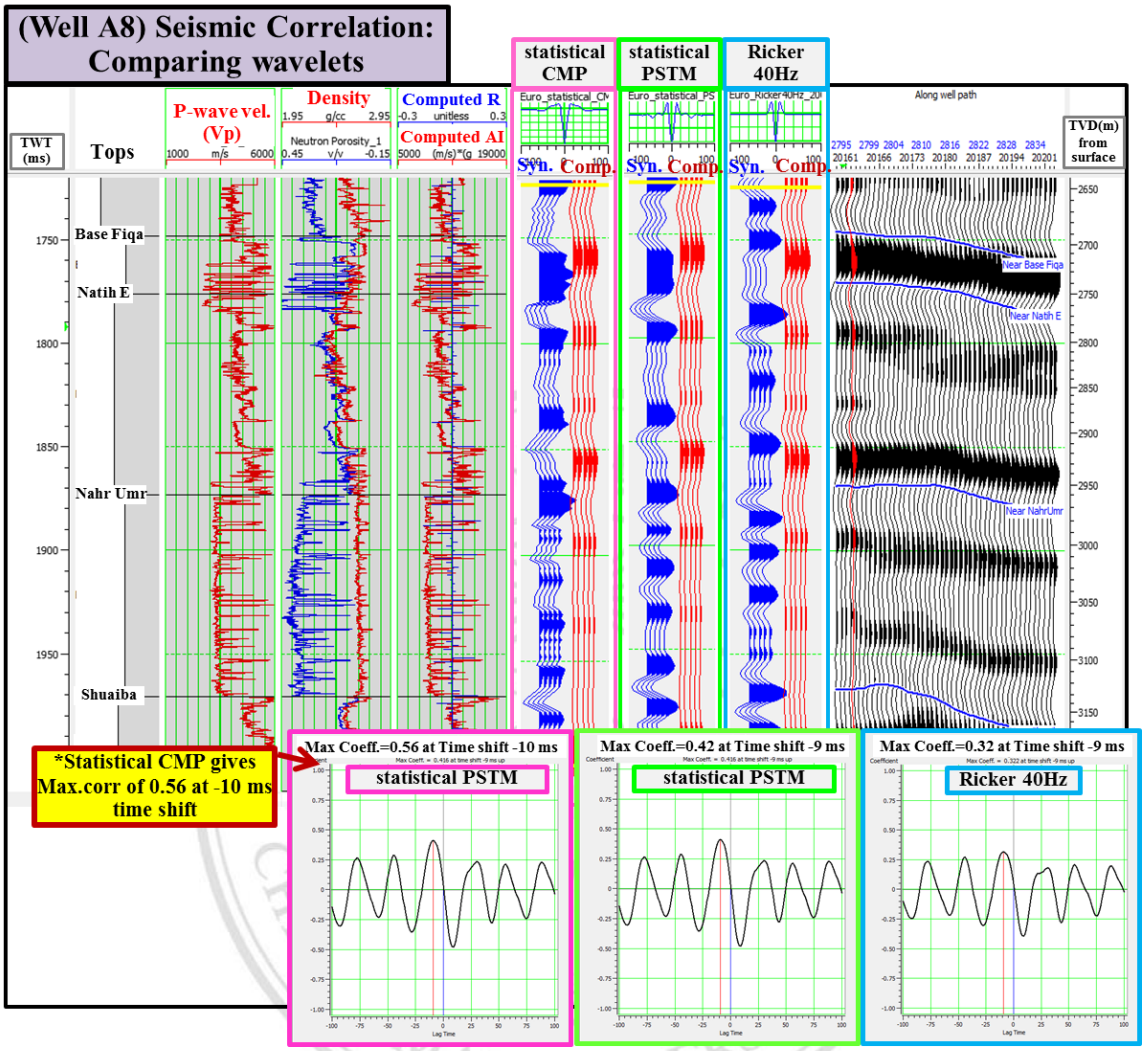

Figure 3.8. The schematic shows the comparison among three seismic correlation panels from three wavelets, which are statistical CMP gathers (pink box), statistical PSTM (light green box), and Ricker 40 Hz (Blue box). The synthetics are in blue traces and the extracted composite are in red traces, and correlation window is from 1725 to 2000 ms TWT.

As used statistical wavelet from pre-stack CMP gathers, the seismic correlation at well A8 can be seen in **Figure 3.9** at which the analysis window is 1725 to 2000 ms TWT. There is the cross correlation plot showing the wavelet phase rotation required at this well (**Figure 3.9**) which is -38 degree.

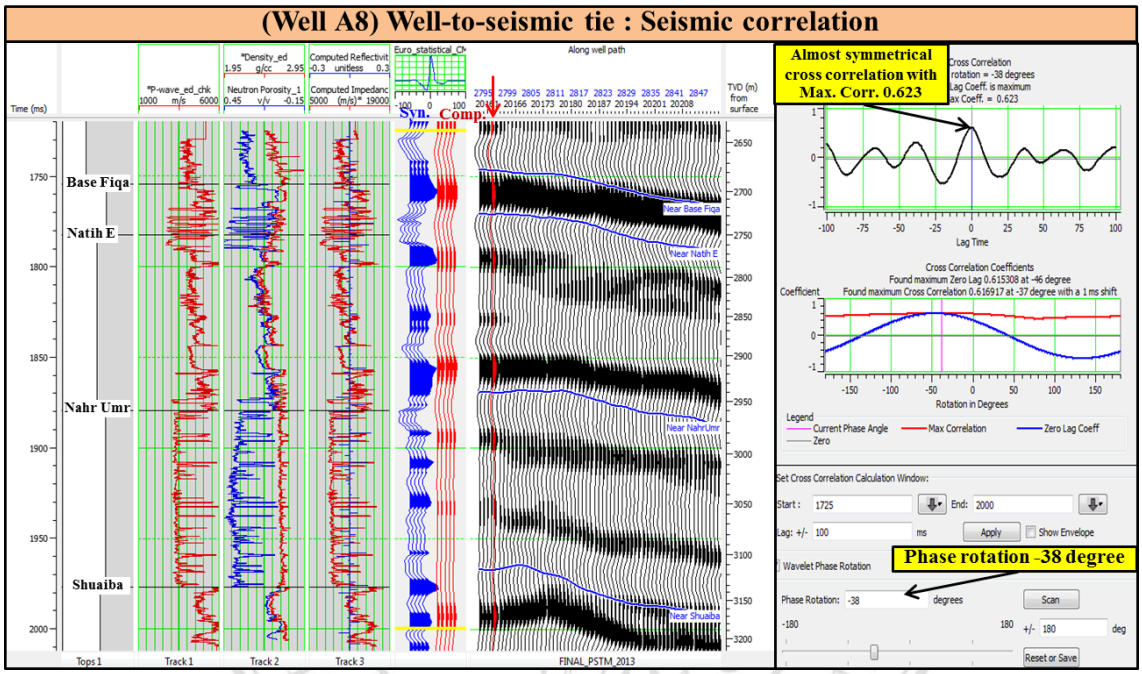

Figure 3.9. The schematic shows the seismic correlation (Left) and its correlation coefficient (Right). The -38 degree of wavelet phase rotation is required at well A8.

After applied the new rotated-phase wavelet of -38 degree, the maximum correlation coefficient is 0.623 as shown in **Figure 3.10**.

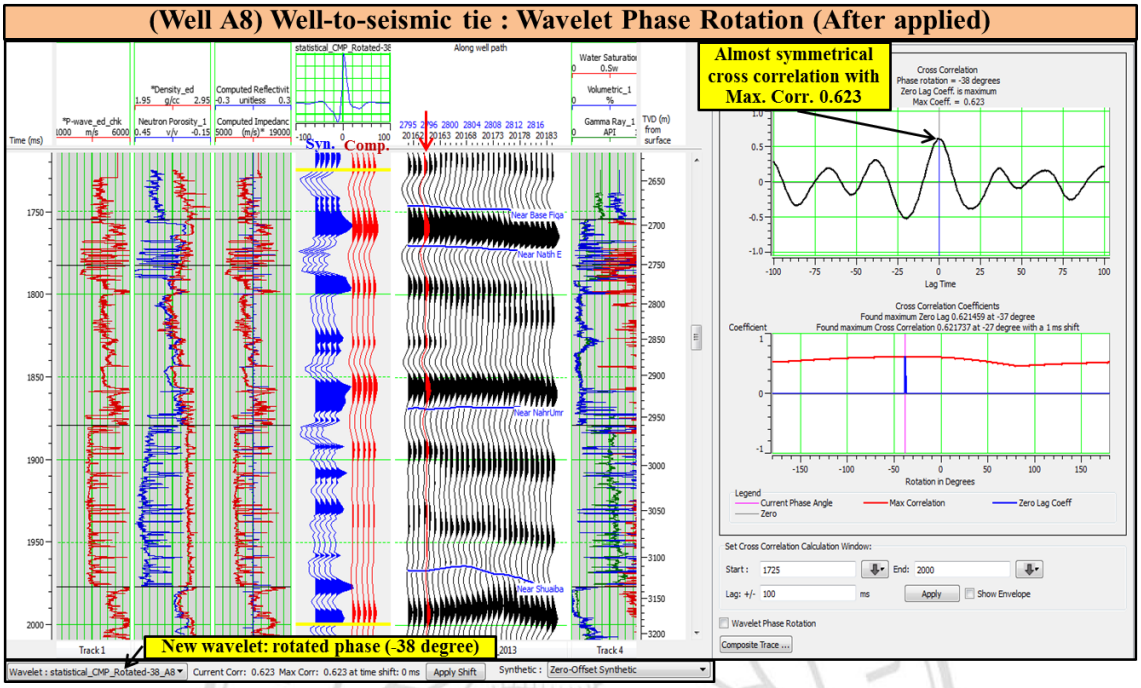

Figure 3.10. The schematic shows the seismic correlation applied new rotated-phase wavelet (Left) and its correlation coefficient of 0.623 (Right).

The well-to-seismic ties were performed at well A1, A2, and A4 to obtain the corrected time-depth and wavelet phase rotation at individual well. As mentioned above, the statistical wavelet from CMP gathers was used at starting point to create synthetics, and then wavelet phase rotation was scanned to determine the new phase rotation at well A1, A2, and A4 (**Figure 3.11, Figure 3.12,** and **Figure 3.13** respectively). The phase rotations to make symmetrical cross-correlation are required at well A1, well A2 and well A4 about -31, -180 and -110 degree respectively.

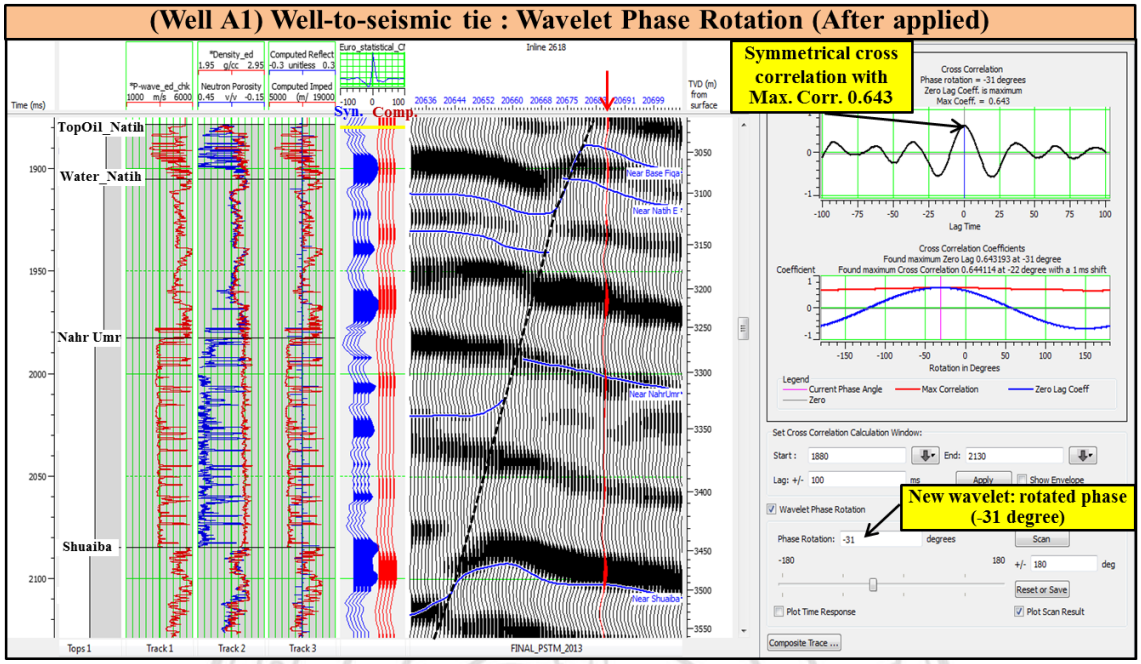

Figure 3.11. The schematic shows the seismic correlation applied new rotated phase wavelet (Left) and its correlation coefficient of 0.643 (Right) at well A1.

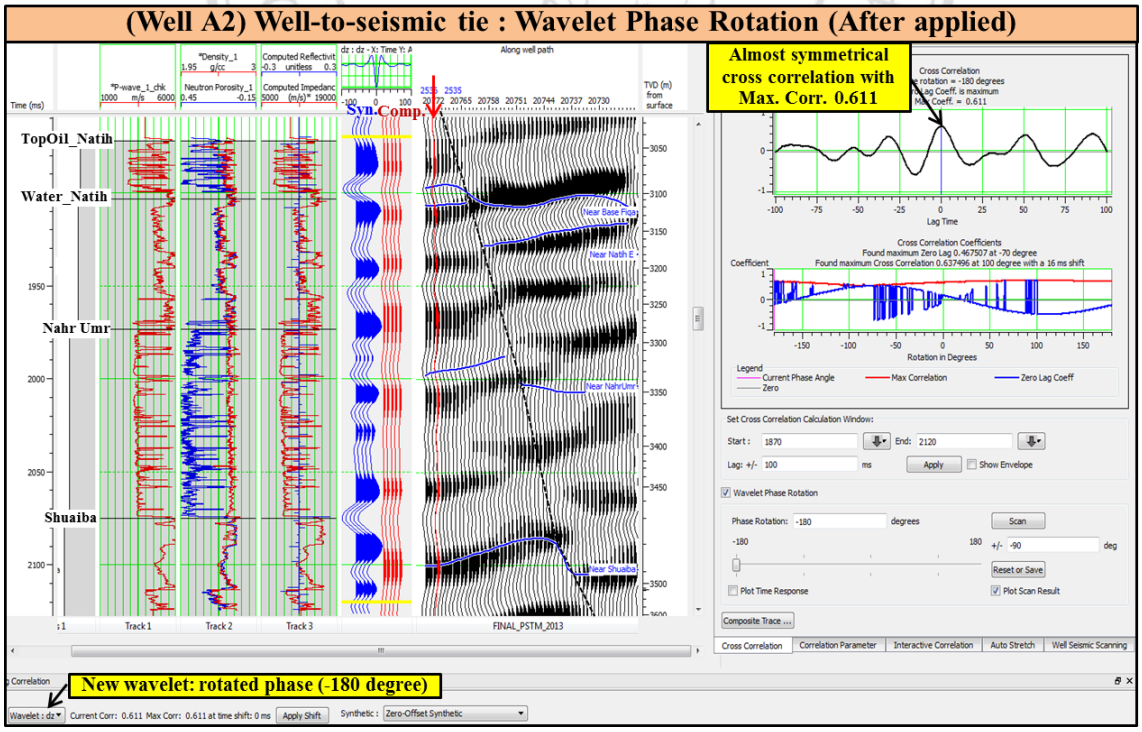

Figure 3.12. The schematic shows the seismic correlation applied new rotated phase wavelet (Left) and its correlation coefficient of 0.611 (Right) at well A2.

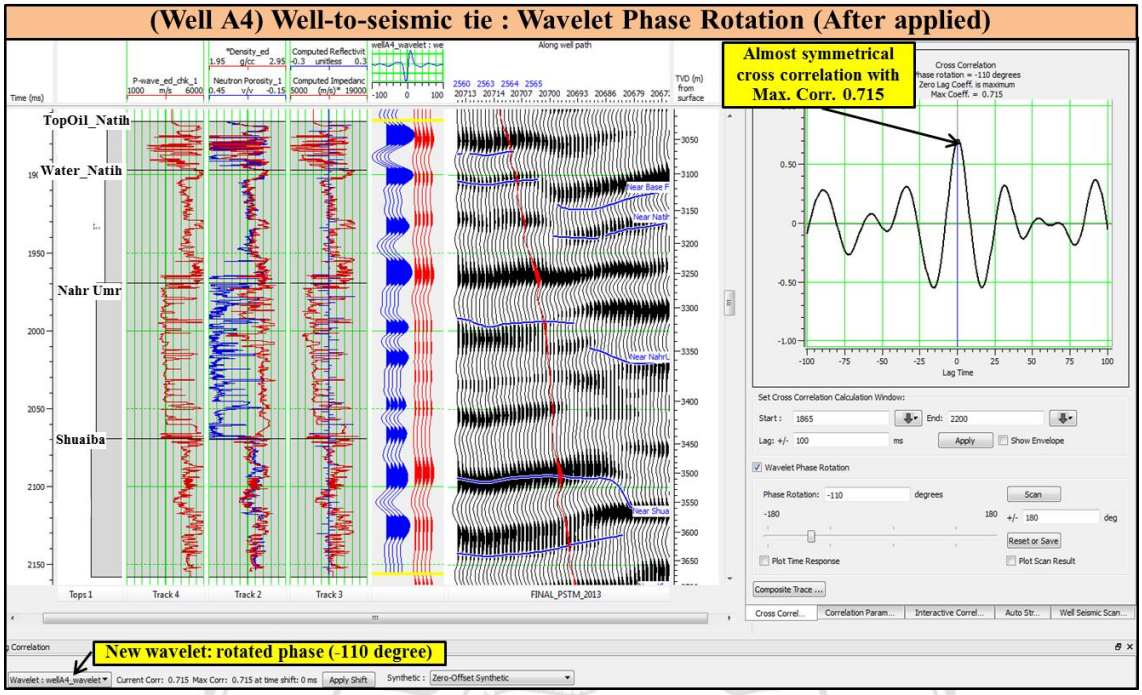

Figure 3.13. The schematic shows the seismic correlation applied new rotated phase wavelet (Left) and its correlation coefficient of 0.715 (Right) at well A4.

After conducting well-to-seismic ties, the new wavelet was extracted with the use of 4-tied wells. Then, this wavelet with averaged -103 degrees of phase was re-done the second time of well-to-seismic ties at all wells in order to achieve better agreement between wells and seismic data which would help to succeed properly in the wavelet extraction for inversion study.

From **Figure 3.14** to Figure **3.17**, there are the schematics of re-do well ties at well A1, A2, A4, and A8 respectively. From those figures it can be concluded that all well-ties using new wavelet from 4-tied wells provide significantly higher correlation coefficient (see **Table 3** for comparison).

The summary of all well ties, including first seismic correlations that had applied the statistical CMP wavelet, and second seismic correlations that had applied the 4-tied wells wavelet can be seen in **Table 3**. The average of maximum correlation involved statistical CMP wavelet from 4 wells is 0.64 and the average from latter is 0.74.

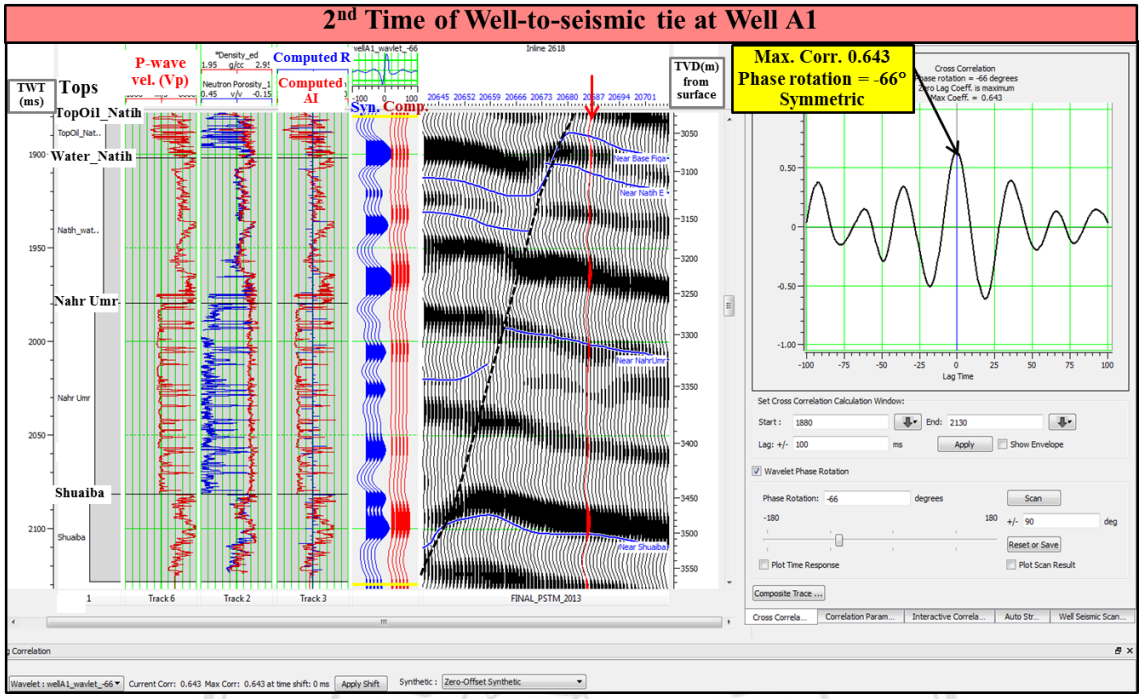

Figure 3.14. The schematic shows re-do seismic correlation applied new rotated phase wavelet (Left) and its correlation coefficient (Right) at well A1.

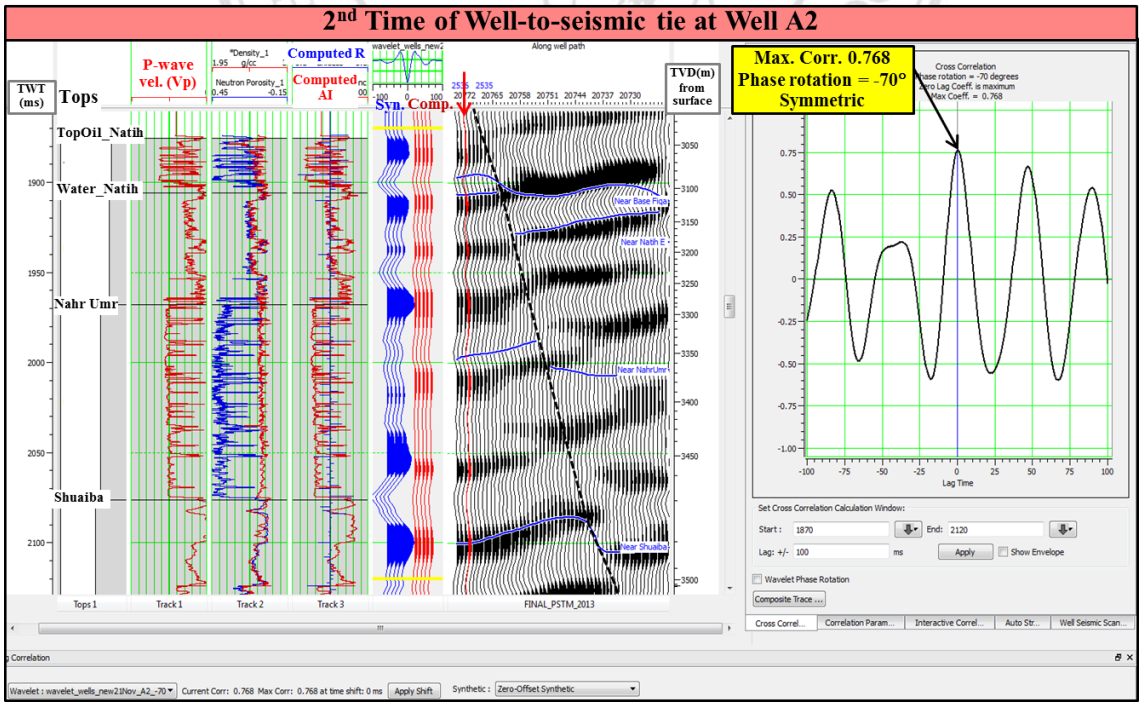

Figure 3.15. The schematic shows re-do seismic correlation applied new rotated phase wavelet (Left) and its correlation coefficient (Right) at well A2.

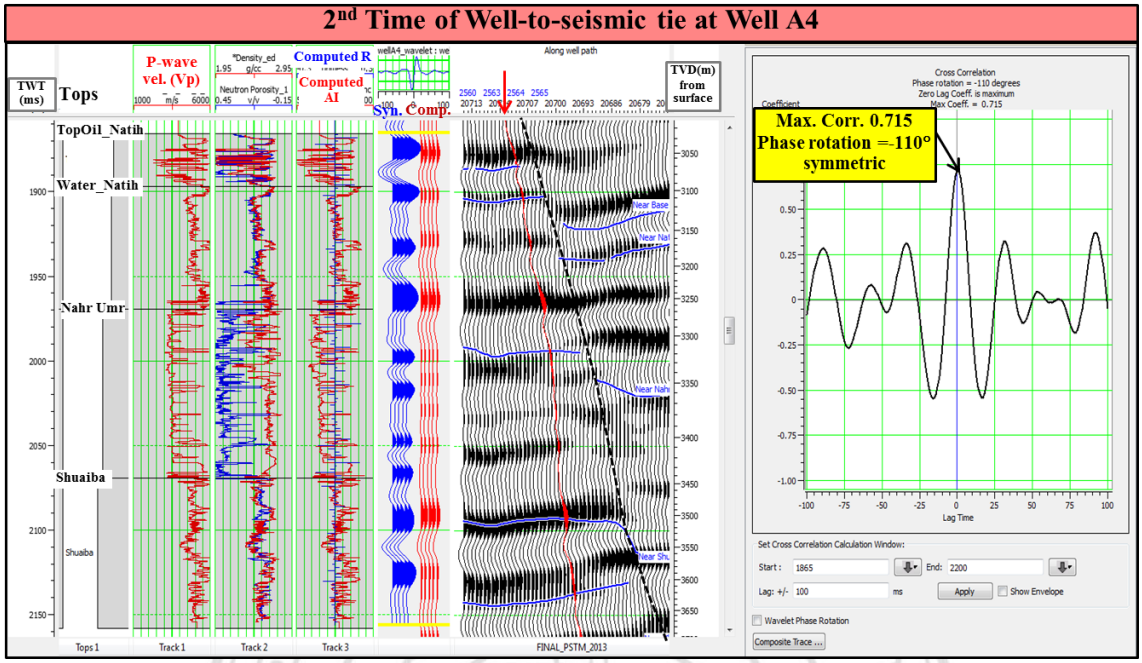

Figure 3.16. The schematic shows re-do seismic correlation applied new rotated phase wavelet (Left) and its correlation coefficient (Right) at well A4.

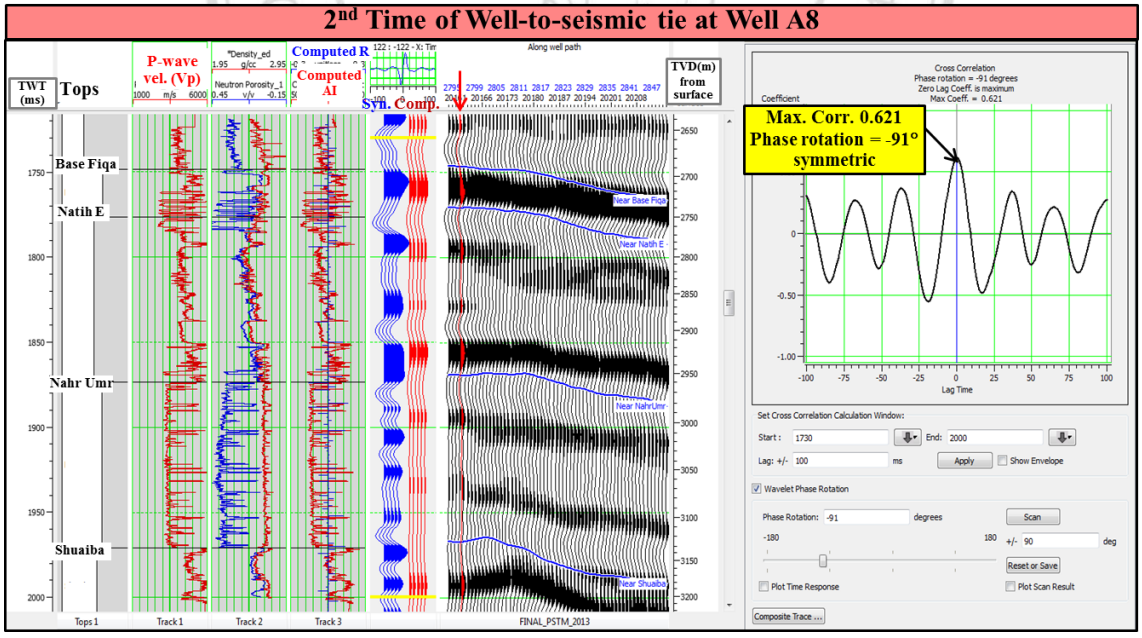

Figure 3.17. The schematic shows re-do seismic correlation applied new rotated phase wavelet (Left) and its correlation coefficient (Right) at well A8.

Table 1. The summary of well-to-seismic ties done in this study.

Well	Action Time	Wavelet used	Max Corr.	Wavelet Phase Rotation (degree)
A1	1	Statistical CMP Wavelet	0.643	-31
	2	Wavelet use 4-tied wells	0.643	-66
A2	1	Statistical CMP Wavelet	0.611	-180
	2	Wavelet use 4-tied wells	0.768	-70
A4	1	Statistical CMP Wavelet	0.680	-110
	2	Wavelet use 4-tied wells	0.715	-110
A8	1	Statistical CMP Wavelet	0.623	-38
	2	Wavelet use 4-tied wells	0.621	-91

3.2.2 Elastic log generation

The main objective of this study is to identify the fluid types by using the application of extended elastic impedance (EEI), therefore the new elastic parameter logs, which are P-wave impedance (Zp), S-wave impedance (Zs), Vp/Vs ratio, Poisson's Ratio, Bulk modulus, Shear modulus, Lambda-Rho ($\lambda\rho$), and Mu-Rho ($\mu\rho$) logs, would be generated to proceed the method of cross correlation. The new elastic parameter logs are as follows.

(1) P-wave impedance (Zp) or acoustic impedance is the product of P-wave velocity (Vp) and density (ρ) as below equation.

$$Zp = Vp * \rho$$ where Vp is in m/s and ρ is in g/cm^3.

(2) S-wave impedance (Zs) is the product of S-wave velocity (Vs) and density (ρ) as below equation.

$$Zs = Vs * \rho$$ where Vs is in m/s and ρ is in g/cm^3.

(3) The ratio of Vp and Vs (Vp/Vs) is the dividing of P-wave velocity (Vp) by S-wave velocity (Vs). The ratio is unitless.

Goodway et al. (1997) introduced to use the Lame' parameters: Lambda (λ) which is incompressibility, related to pore fluid, and Mu (μ) which is rigidity, related to the rock matrix, and density or Rho (ρ) to perform AVO attribute analysis. Based on Goodway et al. (1997)'s study, they could be derived by extracting the P-wave and S-wave reflectivities (Rp and Rs) from pre-stack seismic and inverting them to Zp and Zs. Then the transformation of Zp and Zs into Lambda-Rho ($\lambda\rho$) and Mu-Rho ($\mu\rho$) would be done.

(4) & (5) Lambda-Rho ($\lambda\rho$) and Mu-Rho ($\mu\rho$)'s equations are simply expressed below:

$$\lambda\rho = Zp^2 - 2Zs^2, \quad \text{(Equation 3.1)}$$

$$\text{and } \mu\rho = Zs^2, \quad \text{(Equation 3.2)}$$

where they have the same units: GPa.g/cm^3.

(6) Bulk modulus (k) or incompressibility is the ratio of pressure (P) applied to fractional volume change (ΔV). Bulk modulus in terms of density (ρ), P-wave and S-wave velocities (Vp and Vs) can be written as below equation:

$$k = \rho.(Vp^2 - 4Vs^2/3), \quad \text{(Equation 3.3)}$$

where bulk modulus is in GPa (1 Pa = 1 kg/m.s^2).

(7) Shear modulus (μ) or rigidity is the stress to strain ratio for simple shear which is expressed in terms of density (ρ) and S-wave velocity (Vs) as:

$$\mu = \rho.Vs^2, \quad \text{(Equation 3.4)}$$

where shear modulus is in GPa (1 Pa = 1 kg/m.s^2).

(8) Poisson's ratio (ν) is related to Vp/Vs ratio which can be computed by below equation:

$$\nu = (Vp^2 - 2Vs^2)/2(Vp^2 - Vs^2). \quad \text{(Equation 3.5)}$$

After computed new elastic parameter logs, the log displays for each well are shown in **Figure 3.18** to **Figure 3.21**. In those figures, from left to right, there is gamma ray (GR) log in track 1, and the new elastic parameter logs consisting of Poisson's ratio (PR) in track 2, Vp/Vs in track 3, bulk modulus in track 4, shear modulus in track 5, Lambda-Rho ($\lambda\rho$) in track 6, and Mu-Rho ($\mu\rho$) in track 7.

The oil-filled reservoirs in the Natih formation were highlighted by green boxes at well A1, well A2, and well A4 which characterized at each well by low GR (32, 26 & 19 API), low PR (0.29), low bulk modulus (34, 27 & 30 GPa), low shear modulus (17, 13 & 15 GPa), low $\lambda\rho$ (57, 45 & 49 GPa.g/cm^3), and low $\mu\rho$ (42, 32 & 35 GPa.g/cm^3), indicating by pink arrows (**Figure 3.18 – Figure 3.20**). To compare and contrast between hydrocarbon and non-hydrocarbon zones, the water-bearing reservoirs were highlighted at each well by blue arrows emphasizing the differences in characteristics and higher values (**Figure 3.18 – Figure 3.20**).

Figure 3.21 shows the water-bearing reservoirs in the Natih formation, highlighted by blue arrows, which indicated the higher values of Poisson's ratio (0.33) and Vp/Vs (2.00) than A1, A2, and A4 wells.

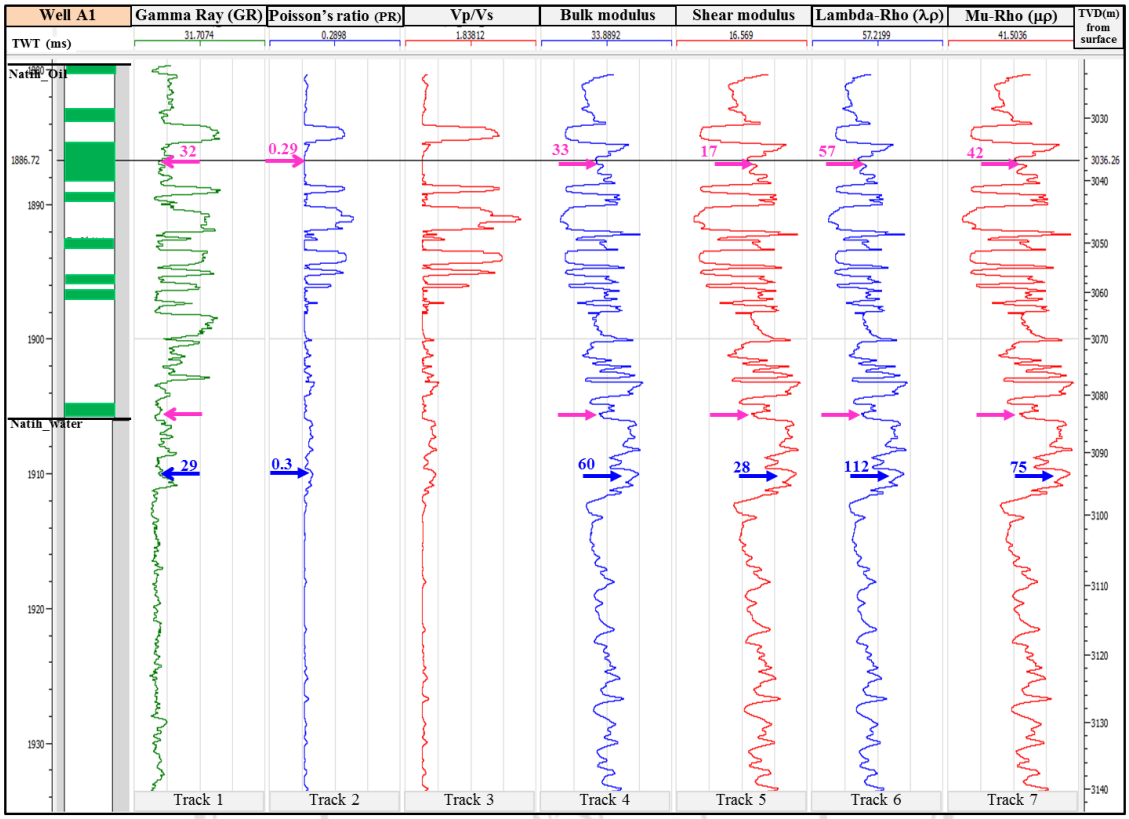

Figure 3.18. The display of well A1 showing the zones of oil-filled reservoirs highlighted by green boxes, which characterized by low GR (32 API), low PR (0.29), low bulk modulus (34 GPa), low shear modulus (17 GPa), low λρ (57 GPa.g/cm^3), and low μρ (42 GPa.g/cm^3) indicating by pink arrows. The blue arrows highlighted non-hydrocarbon zone.

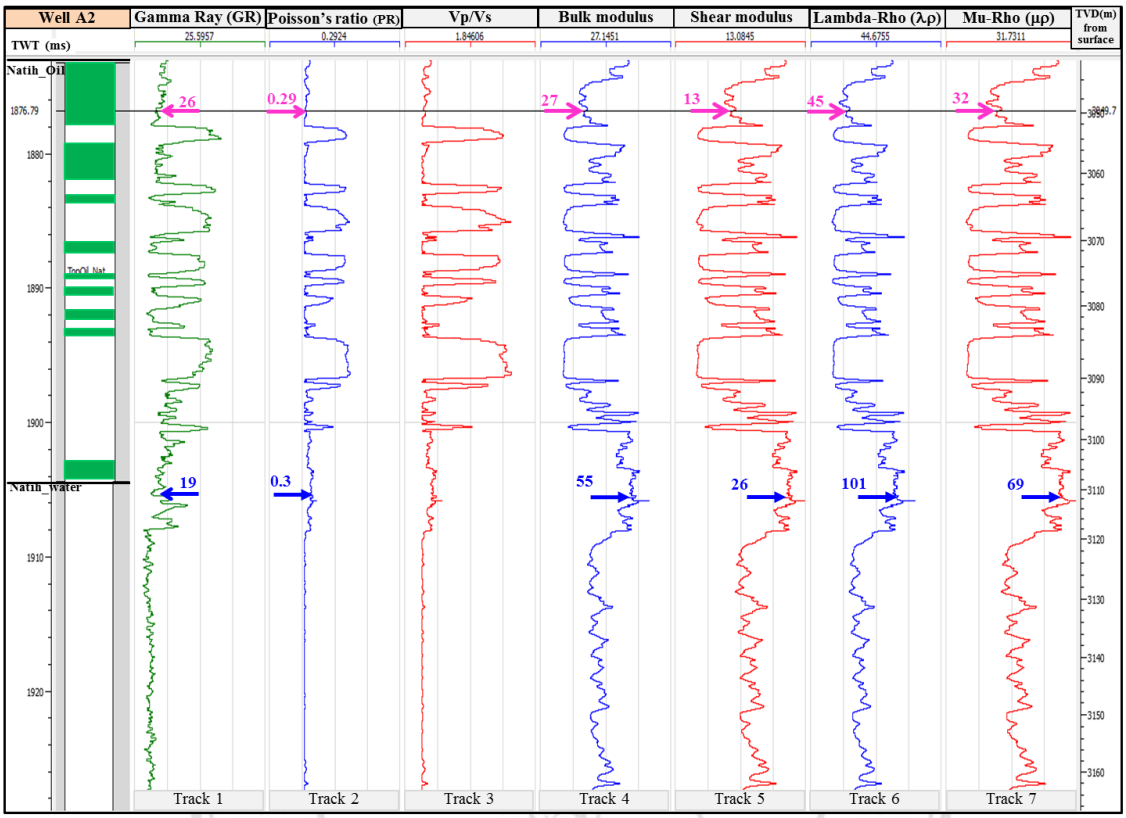

Figure 3.19. The display of well A2 showing the zones of oil-filled reservoirs highlighted by green boxes, which characterized by low GR (26 API), low PR (0.29), low bulk modulus (27 GPa), low shear modulus (13 GPa), low λρ (45 GPa.g/cm^3), and low μρ (32 GPa.g/cm^3) indicating by pink arrows. The blue arrows highlighted non-hydrocarbon zone.

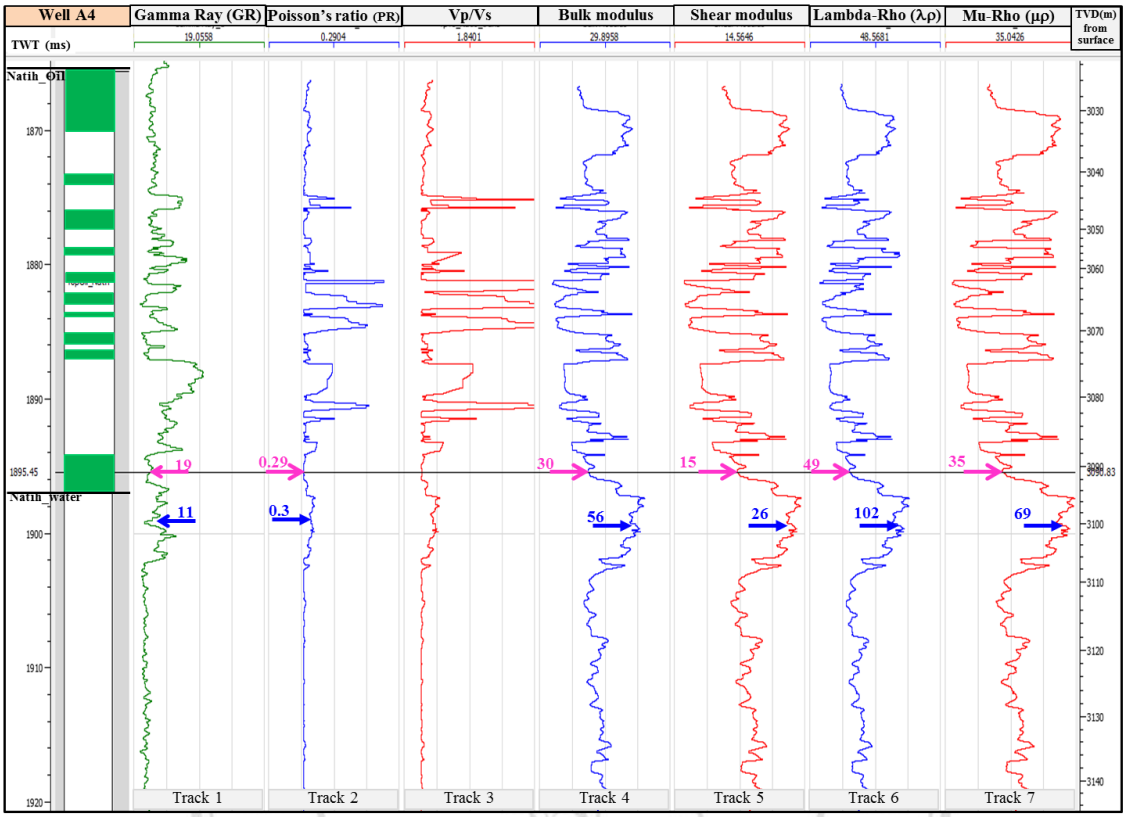

Figure 3.20. The display of well A4 showing the zones of oil-filled reservoirs highlighted by green boxes, which characterized by low GR (19 API), low PR (0.29), low bulk modulus (30 GPa), low shear modulus (15 GPa), low λρ (49 GPa.g/cm^3), and low μρ (35 GPa.g/cm^3) indicating by pink arrows. The blue arrows highlighted non-hydrocarbon zone.

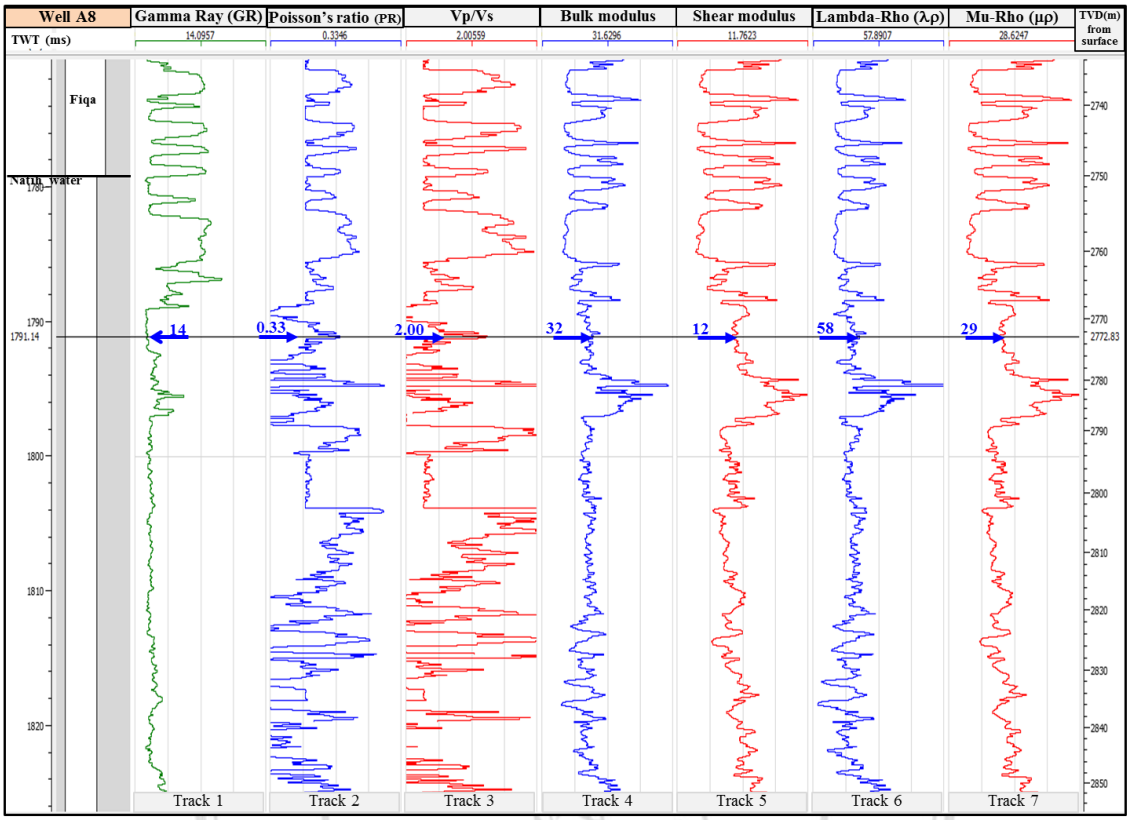

Figure 3.21. The log display of well A8 showing gamma ray and a number of new elastic parameter logs in which the blue arrows indicated curve values of water-bearing reservoir in the Natih formation.

3.3 AVO gradient analysis

Amplitude versus offset (AVO) is the comparison of seismic amplitude changes across the offset range which can normally be separated into near (zero), mid, and far offsets. To preceed the computation, the offset domain would be transformed to the angle domain. The common linear approximation of AVO is three-terms of Aki-Richards (1980), see Equation 2.3, which accounts for the differences between the P-wave and S-wave velocities (Vp and Vs), and density (ρ) over the offset (angle of incidence, θ).

The basic concept of AVO was illustrated in **Figure 3.22**, at which the increases of source-receiver offset is equivalent to the increases of angle of incidence (θ), and the use of above approximation (Aki-Richards, 1980) can compute seismic amplitudes across angle range and then plot on the amplitude versus $\sin^2\theta$. The intercept, A is the trend of the amplitude measurements meets the zero-offset line, which is equivalent to zero-offset reflectivity (R), thus symbol of R(0) might also be used. The gradient, B is calculated as the slope of the change in amplitude with $\sin^2\theta$.

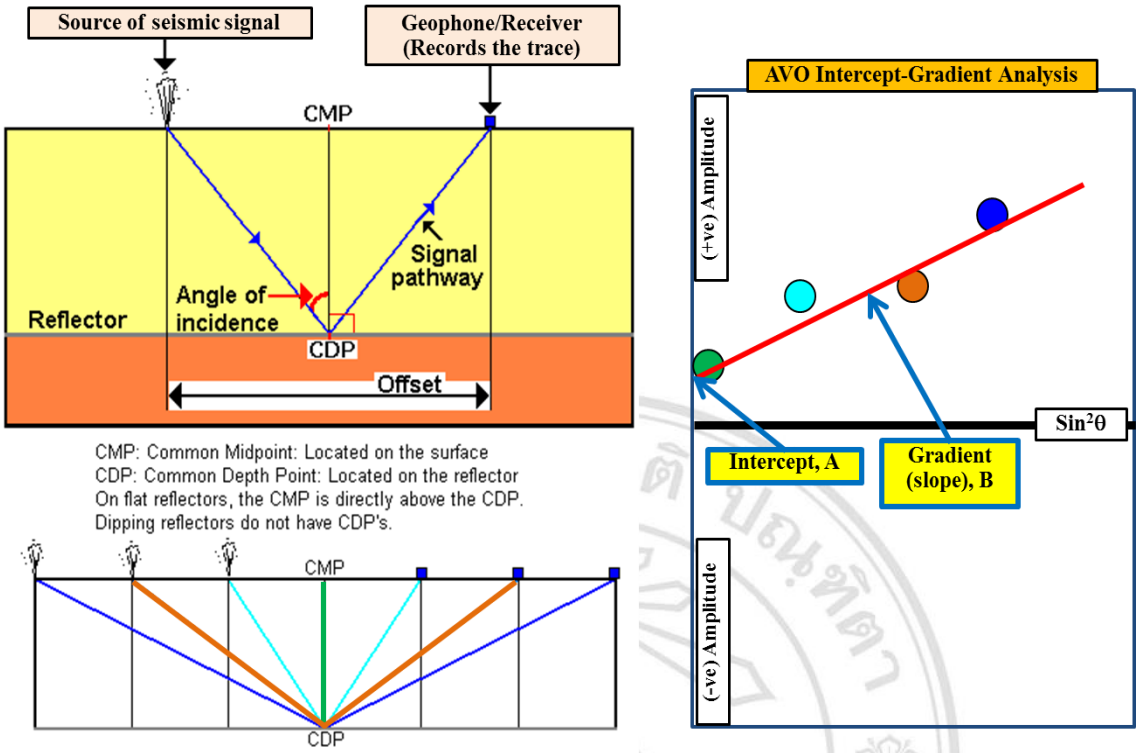

Figure 3.22. The basic concept of AVO includes: on the left, the schematic of source-receiver offsets (modified from Hampson and Russell, 2015) and on the right, AVO intercept-gradient analysis.

To describe the AVO responses, there are a few terms related to their characteristics which are positive (+ve) or negative (-ve) AVO and positive (+ve) or negative (-ve) gradient (**Figure 3.23-A**.), and the conventional terms of a number of classes: class I, II, III, and IV (**Figure 3.23-B**.).

On the AVO plot, the positive (+ve) gradients are tilted from upper right to lower left whereas the negative (-ve) gradients are tilted from upper left to lower right (**Figure 3.23-A**.). When the increase of the absolute amplitude value (magnitude) with increasing offset (or angle) is observed, it is called positive (+ve) AVO, or sometimes called rising AVO at which this term can be applied to either positive or negative amplitudes. The negative (-ve) AVO would be described where the decrease of the absolute amplitude value (magnitude) with increasing offset (or angle).

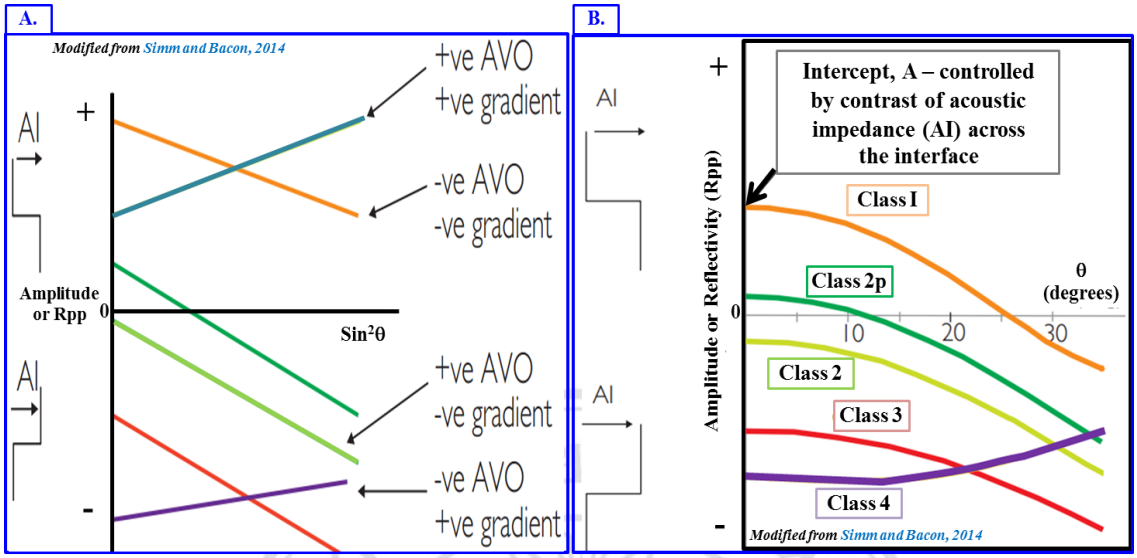

Figure 3.23. (A.), the terminology of AVO and (B.), the AVO classifications (modified from Simm and Bacon, 2014).

The conventional terms describing AVO responses are a number of classes which are class I, class II and IIp, class III, and class IV. The characteristics and definition of AVO responses can be seen in **Figure 3.23-B** and **Table 4**.

Table 2. The summary of AVO classes and definitions.

Class	Gradient	Absolute Amplitudes	Notes
I	-	Far < A	+ve A, may have phase reversal
IIp	-	Far > A	+ve A, phase reversel
II	-	Far > A	Low amplitude at A
III	-	Far > A	Relatively high amplitude at A
IV	+	Far < A	Very high amplitude at A

The AVO gradient analysis was performed at well A8, well A1, well A2, and well A4 corresponding to target time of 1784, 1918, 1902, and 1898 ms TWT respectively (**Figure 3.24 – Figure 3.27**). Three-term Aki-Richards (Aki-Richards, 1980), Equation 2.3, was applied to derive the amplitude changes across angles which were plotted in the amplitude versus $\sin^2\theta$.

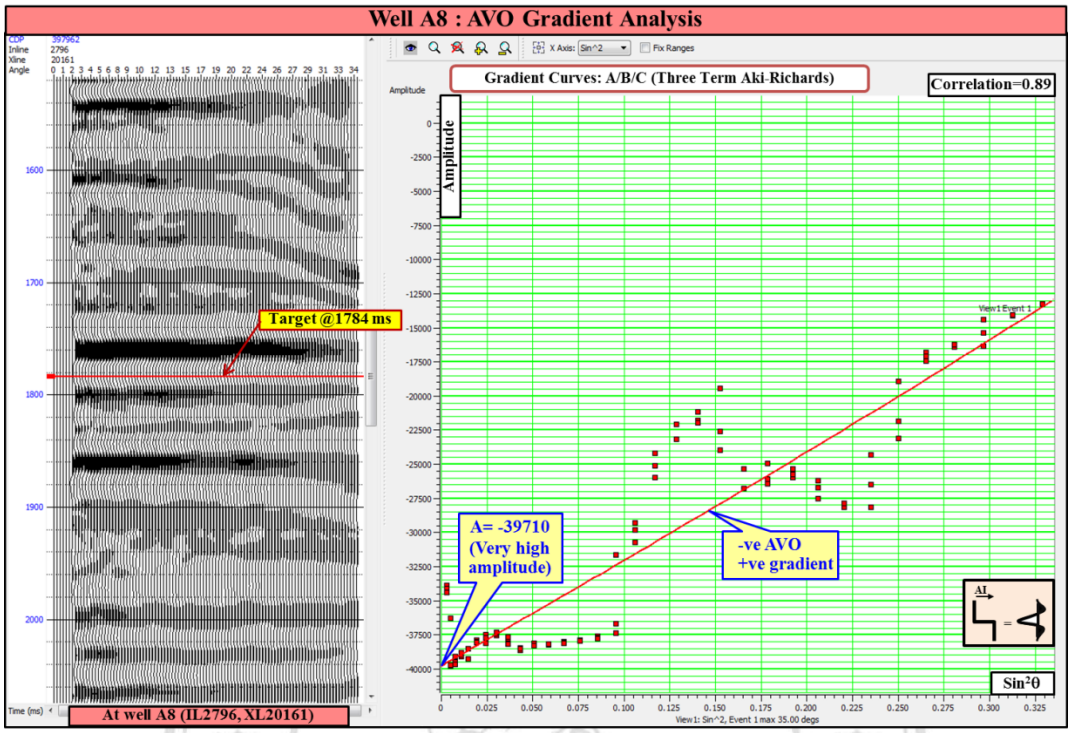

Figure 3.24. The AVO plot of well A8 shows very high amplitude of intercept (A), negative AVO and gradient. It was interpreted as Class I (Class 1).

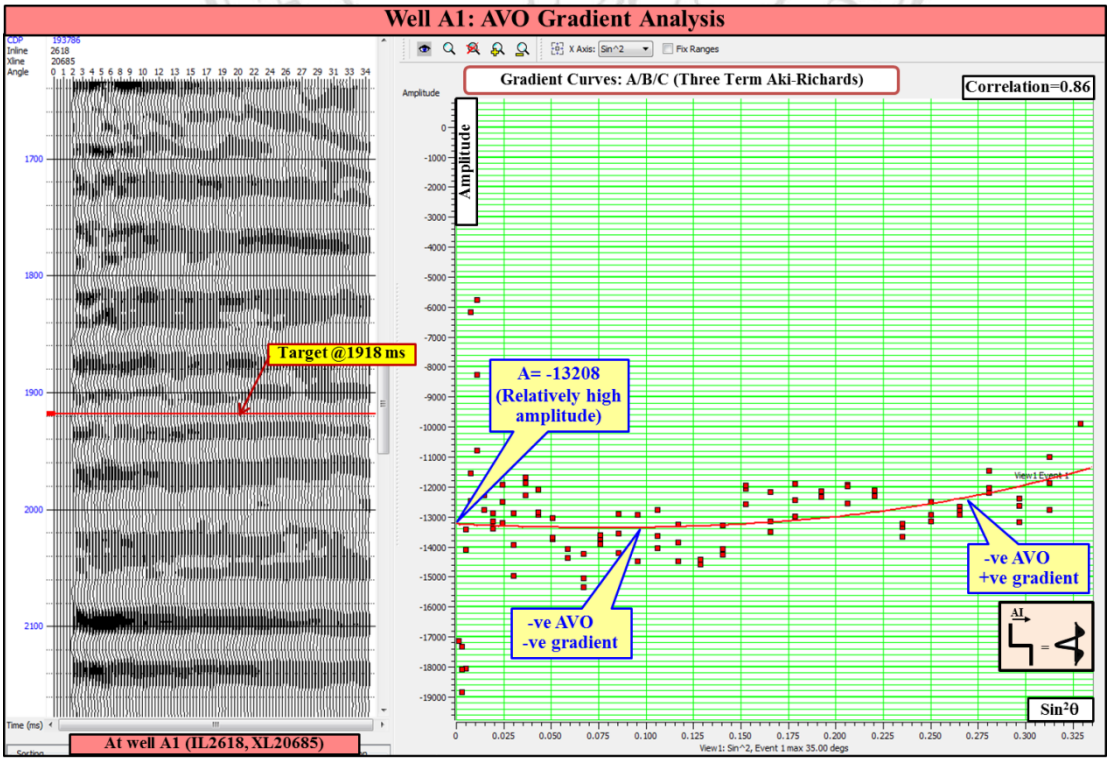

Figure 3.25. The AVO plot of well A1 shows relatively high amplitude of intercept (A), and two sets of AVO responses and gradients. It was interpreted as Class I (Class 1).

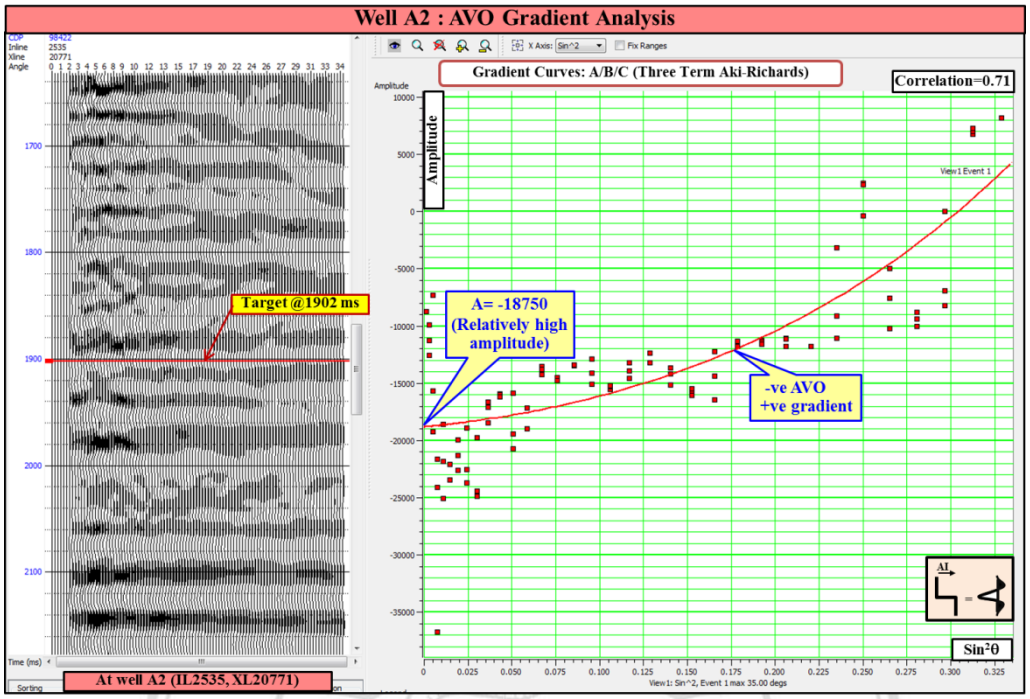

Figure 3.26. The AVO plot of well A2 shows relatively high amplitude of intercept (A), negative AVO and gradient. It was interpreted as Class I (Class 1).

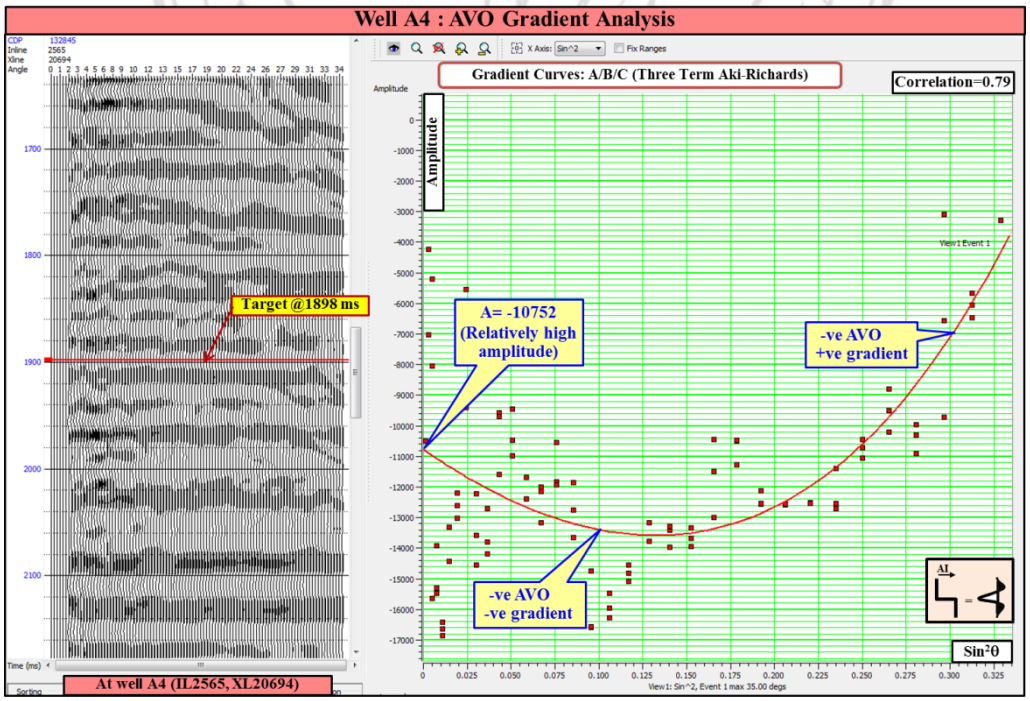

Figure 3.27. The AVO plot of well A4 shows relatively high amplitude of intercept (A), and two sets of AVO responses and gradients. It was interpreted as Class I.

Based on assumption of European polarity, from AVO plots of all wells, they show significantly the AVO Class I having negative gradient, very high to relatively high amplitude of intercept A, and the amplitude of far offset (increasing offset/angle) is less than intercept A (**Figure 3.24 – 3.27**).